Preprint typeset using LaTeX style emulateapj v. 5/2/11

HIGH ANGULAR MOMENTUM HALO GAS: A FEEDBACK AND CODE–INDEPENDENT PREDICTION OF LCDM

Kyle R. Stewart[1], Ariyeh H. Maller[2,3], Jose Oñorbe[4], James S. Bullock[5,6], M. Ryan Joung[7], Julien Devriendt[8], Daniel Ceverino[9], Dušan Kereš[10], Philip F. Hopkins[11], and Claude-André Faucher-Giguère[12]

ABSTRACT

We investigate angular momentum acquisition in Milky Way sized galaxies by comparing five high resolution zoom–in simulations, each implementing identical cosmological initial conditions, but utilizing different hydrodynamic codes: `Enzo`, `Art`, `Ramses`, `Arepo`, and `Gizmo-PSPH`. Each code implements a distinct set of feedback and star formation prescriptions. We find that while many galaxy and halo properties vary between the different codes (and feedback prescriptions), there is qualitative agreement on the process of angular momentum acquisition in the galaxy's halo. In all simulations, cold filamentary gas accretion to the halo results in ~ 4 times more specific angular momentum in cold halo gas ($\lambda_{\rm cold} \simeq 0.15$) than in the dark matter halo. At $z > 1$, this inflow frequently results in the formation of transient cold flow disks—large co–rotating gaseous structures in the halo of the galaxy that are fueled, aligned, and kinematically connected to filamentary gas infall along the cosmic web. Due to the qualitative agreement among disparate simulations, we conclude that the buildup of high angular momentum halo gas and the transitory formation of cold flow disks are robust predictions of LCDM galaxy formation. A growing body of observational evidence suggests that this process is borne out in the real universe.

Subject headings: galaxies:formation—halos—evolution — methods:numerical—hydrodynamic—simulation

1. INTRODUCTION

In the standard Lambda Cold Dark Matter (LCDM) picture of galaxy formation, gas accreting onto a growing dark matter halo shock-heats to the virial temperature of the halo, giving the gas time to virialize and eventually cool out of the hot gaseous halo and sink onto the central galaxy (Rees & Ostriker 1977; Silk 1977; White & Rees 1978; White & Frenk 1991; Maller & Bullock 2004). Under this picture of galaxy growth, it is expected that the resulting angular momentum distribution of galaxies should mimic the spin of their dark matter, resulting in rotationally supported galaxy disks (and presumably hot gaseous halos as well) that are proportional to the spin of the dark matter halo (Fall & Efstathiou 1980; Mo et al. 1998), which has been well studied in dissipationless N-body simulations (e.g. Bullock et al. 2001; Vitvitska et al. 2002; Maller et al. 2002; Avila-Reese et al. 2005; D'Onghia & Navarro 2007; Bett et al. 2010; Muñoz-Cuartas et al. 2011; Ishiyama et al. 2013; Trowland et al. 2013; Kim et al. 2015).

However, recent advances in hydrodynamic simulations and galaxy formation theory have increasingly emphasized the importance of "cold flows"—gas accretion onto galaxy halos via filamentary streams with cooling times shorter than the compression time for establishing a stable shock[13], either when the halo is below a critical mass threshold, or even for massive halos at sufficiently high redshift (e.g. Binney 1977; Kereš et al. 2005; Dekel & Birnboim 2006; Ocvirk et al. 2008; Brooks et al. 2009; Dekel et al. 2009; Faucher-Giguère & Kereš 2011; Faucher-Giguère et al. 2011; Stewart et al. 2011a; van de Voort et al. 2011; Hobbs et al. 2015; van de Voort et al. 2015). In the cold flow paradigm, gas that is accreted in the cold mode tends to have specific angular momentum considerably higher than the dark matter (Chen et al. 2003; Sharma & Steinmetz 2005; Kereš et al. 2009; Kereš & Hernquist 2009; Agertz et al. 2009; Brook et al. 2011a; Stewart et al. 2011b; Kimm et al. 2011), inconsistent with the previous picture of galaxy angular momentum buildup. The resulting angular momentum of the stellar disk may be rather different than that of the accreted gas because of feedback effects (Maller & Dekel 2002; Brook et al. 2011b).

[1] Department of Natural and Mathematical Sciences, California Baptist University, 8432 Magnolia Ave., Riverside, CA 92504, USA
[2] Department of Physics, New York City College of Technology, 300 Jay St., Brooklyn, NY 11201, USA
[3] Department of Astrophysics, American Museum of Natural History, Central Park West at 79th Street, New York, NY 10024, USA
[4] Max-Planck-Institut fr Astronomie, Knigstuhl 17, D-69117 Heidelberg, Germany
[5] Center for Cosmology, Department of Physics and Astronomy, The University of California at Irvine, Irvine, CA, 92697, USA
[6] Center for Galaxy Evolution, Department of Physics and Astronomy, The University of California at Irvine, Irvine, CA, 92697, USA
[7] Department of Astronomy, Columbia University, New York, NY 10027, USA
[8] Department of Physics, University of Oxford, The Denys Wilkinson Building, Keble Road, Oxford OX1 3RH, UK
[9] Zentrum fur Astronomie der Universitat Heidelberg, Institut fur Theoretische Astrophysik, Albert-Ueberle-Str. 2, 69120 Heidelberg, Germany
[10] Department of Physics, Center for Astrophysics and Space Sciences, University of California at San Diego, 9500 Gilman Drive,La Jolla, CA 92093, USA
[11] California Institute of Technology, 1200 E. California Boulevard, Pasadena, CA 91125, USA
[12] Department of Physics and Astronomy and CIERA, Northwestern University, 2145 Sheridan Road, Evanston, IL 60208, USA

[13] Some recent moving–mesh simulations have called into question whether these cold streams deliver unshocked gas *to the galaxy* without heating in the inner regions of the halo (e.g. Torrey et al. 2012; Nelson et al. 2013, 2015, 2016). As our focus in this work is on gas accretion into the *halo*, not the eventual transition from the halo to the galaxy, this distinction should have minimal impact on topics discussed here.

As a result of this changing paradigm for cosmological gas accretion and galaxy growth, a new scenario of angular momentum acquisition in galaxies and galaxy halos seems to be emerging. In this picture (Stewart et al. 2011b; Kimm et al. 2011; Pichon et al. 2011; Codis et al. 2012; Danovich et al. 2012; Stewart et al. 2013; Codis et al. 2015; Danovich et al. 2015; Prieto et al. 2015; Tillson et al. 2015) the particularly high angular momentum of cold flow gas is related to its coherent, filamentary origin, coupled with the specific geometry of the cosmic web in the environment of a given galaxy. These filamentary cold flows deliver significant angular momentum to galaxy halos, with the cold gas orbiting for $\sim 1-2$ dynamical times before spiraling into the central galaxy. At any given time, galaxy disks typically have lower spin than halo gas owing to the fact that the specific angular momentum of infalling material increases with time. Halo gas is "younger" and this correlates with higher spin.

Importantly, this scenario is predictive. The high–spin halo gas is often (but not always) coherent in its spin direction. It often forms a thick planar structure of high angular momentum cool gas that co–rotates with the central disk. Throughout this work, we will refer to this transient structure as a "cold flow disk," though we note that this gas is not rotationally supported—it typically spirals in within ~ 2 dynamical times. Nor are these structures especially thin or perfectly aligned with the orientation of the the galactic disk. The "disk" here refers to how the accreting cold-mode gas shows observational signs of coherent rotation along a preferred plane.

Encouragingly, an increasing number of observations have begun to demonstrate the abundance of high angular momentum material in galaxy halos, qualitatively consistent with this emerging theoretical picture. In the local universe, some of these observations include detection of high angular momentum extended H I disks and XUV disks (Oosterloo et al. 2007; Christlein & Zaritsky 2008; Sancisi et al. 2008; Lemonias et al. 2011; Holwerda et al. 2012), as well as low metallicity high angular momentum gas (presumably from fresh accretion) in polar ring galaxies (Spavone et al. 2010). There is even indication that local extended H I disks may be environmentally dependent on the galaxy's filamentary environment (Courtois et al. 2015). At moderate redshift ($z \sim 0.5$–1.5) numerous absorption line studies of the circumgalactic medium of galaxies have begun to emphasize the bi–modal properties of absorbers, where absorption along the galaxy's major axis tends to show high angular momentum (co–rotating) inflow, and absorption along the galaxy's minor axis shows observational signatures of outflow (Kacprzak et al. 2010, 2012a,b; Bouché et al. 2012, 2013; Crighton et al. 2013; Nielsen et al. 2015; Diamond-Stanic et al. 2015; Bouché et al. 2016). At higher redshift ($z \sim 2$–3) kinematic studies of Ly–α "blobs" have observed large scale rotation consistent with high angular momentum cold gas accretion (Martin et al. 2014; Prescott et al. 2015). There are also recent detections of massive protogalactic gaseous disks kinematically linked to gas inflow along a cosmic filaments, strikingly similar to the theoretical "cold flow disk" structure (Martin et al. 2015, 2016).

In this context, it is important that we ascertain how robust the predictions of these cosmological simulations are—a difficult task considering that many properties of simulated galaxies depend sensitively on the implementation of uncertain subgrid physics models such as gas cooling, star formation, radiation pressure, and supernova feedback (e.g., Thacker & Couchman 2000; Kay et al. 2002; Scannapieco et al. 2012; Gnedin et al. 2011; Piontek & Steinmetz 2011; Martizzi et al. 2012; Agertz et al. 2013; Vogelsberger et al. 2013; Vogelsberger et al. 2014; Marasco et al. 2015; Genel et al. 2015; Ceverino et al. 2014; Agertz & Kravtsov 2015). In addition, even with identical subgrid implementations, there are inherent numerical advantages and disadvantages between different hydrodynamic code implementations—for example, Lagrangian smoothed particle hydrodynamic (SPH) versus Eulerian grid codes—that result in artificial differences between galaxies simulated with different codes (e.g., Morris 1996; Agertz et al. 2007; Wadsley et al. 2008; Cullen & Dehnen 2010; Hahn et al. 2010; Springel 2010; Hopkins 2015; Richardson et al. 2016).

In order to test the validity of the emerging cold flow picture of angular momentum acquisition we must ascertain the dependency of these predictions on the use of different numerical techniques and a variety of cutting–edge subgrid physics models. In this paper, we run five hydrodynamic zoom-in simulations of a Milky Way sized galaxy, each with identical cosmological initial conditions but with different codes: `Enzo`, `Ramses`, `Art`, `Arepo`, and `Gizmo-PSPH`, each implemented with current subgrid physics models. In order to ensure uniform analysis for different hydrodynamic codes, we utilize the analysis software `yt` (which allows a single analysis routine to be run on different code architectures; Turk et al. 2011) to explore the angular momentum content of halo gas and whether or not the expected "cold flow disk" prediction is robust across these disparate platforms. We introduce the simulations in §2, present our main results from the comparison §3–§5, finding that the same qualitative picture of high angular momentum halo gas and frequent formation of the cold flow disk phenomenon is present in all simulations, a seemingly natural consequence of filamentary gas accretion in LCDM. We discuss the implications of these results and the growing observational evidence of their existence in §6 and summarize and conclude in §7.

2. THE SIMULATIONS

2.1. *Overview*

The simulations used in this paper are all part of the Scylla Multi–Code Comparison Project.This project resimulates a Milky Way halo mass zoom–in simulation (originally performed by Ryan Joung with `Enzo` in Joung et al. 2012) using other cosmological hydrodynamic codes. The codes are all run with their current[14] subgrid models in order to compare state of the art simulations across codes. Thus the project is much like the Aquilla code comparison (Scannapieco et al. 2012) but with higher resolution. Our resolution is similar to the Agora code comparison project (Kim et al. 2014), but that project is seeking to use uniform physics while we

[14] Though, inevitably, there are bound to be recent improvements to some of the subgrid models during the time it took to run the simulations, analyze and publish the results.

Table 1
SIMULATION CODE DETAILS

	`Enzo`	`Art`	`Ramses`	`Arepo`	`Gizmo-PSPH`
Gravity Solver	FFT in the root grid	multilevel particle mesh	multigrid particle mesh	tree multipole expansion particle mesh	tree multipole expansion particle mesh
Hydrodynamics Solver	3rd–order piecewise parabolic method	2nd–order Godunov method	2nd–order MUSCL scheme	2nd–order MUSCL scheme†	Pressure–energy SPH
High Res. $m_{\rm DM}^{\ddagger}$	$1.75 \times 10^5 M_\odot$	$1.75 \times 10^5 M_\odot$	$1.75 \times 10^5 M_\odot$	$1.75 \times 10^5 M_\odot$	$1.75 \times 10^5 M_\odot$
Grav. Softening [h^{-1} comoving pc]	95 (DM, gas)	95 (DM, gas)	95 (DM, gas)	95 (DM, gas)	95 (DM), 14 (gas)
SF Threshold	0.04 cm^{-3}	1 cm^{-3}	1 cm^{-3}	0.13 cm^{-3}	5 cm^{-3} + self–grav. + molecular
SF Efficiency	$\epsilon = 0.03$	$\epsilon = 0.03$	$\epsilon = 0.03$	$t_{SFR} = 2.2$ Gyr	$\epsilon = 1$ (in self–grav., molecular gas)
Stellar Feedback⋆	Thermal	Thermal & Rad.	Kinetic	Kinetic	Mixed [see text]
Temperature Floor	10 K	300 K	100 K	500 K	10 K
UV Background	HM96 (increased Gaussian width)	HM96	HM96	FG09	FG09
Reionization	$z = 6$	$z = 7$	$z = 10$	$z = 10$	$z = 10$

HM96 — Haardt & Madau (1996)
FG09 — Faucher-Giguère et al. (2009)
† Subsequent versions of `Arepo` have switched to a different time integration (Pakmor et al. 2016) using Heuns method
‡ For Lagrangian codes, high resolution gas particle mass is $3.3 \times 10^4 M_\odot$
⋆ See text for detailed descriptions of feedback models.

are running each code as it has been used for other science papers. The codes used here are `Enzo`, `Art`, `Ramses`, `Arepo` and `Gizmo-PSPH`. For all runs the cosmology, dark matter particle mass and box size are identical—the box is 25 Mpc/h across with a much smaller region simulated at high resolution, using dark matter particles of mass $1.75 \times 10^5 M_\odot$. All adaptive mesh refinement codes reach the same maximum refinement of 95 h^{-1} comoving pc, which is identical to the force resolution of the Lagrangian codes, with the exception of gas particles in `Gizmo-PSPH`, which uses an adaptive gravitational softening with a minimum value of 14 h^{-1} comoving pc. A flat cosmology consistent with WMAP5 (Komatsu et al. 2009) is used throughout, with $\Omega_m = 0.279$, $\Omega_\Lambda = 0.721$, $\Omega_b = 0.046$, $h = 0.70$, $\sigma_8 = 0.82$ and $n_s = 0.96$.

The initial conditions for the original `Enzo` run (Joung et al. 2012) were generated with the code `Grafic`[15] (Bertschinger 2011) with a starting redshift of $z = 99$. The same code with the same seed was used to generate the initial conditions for the `Ramses` run. For all other runs the dark matter particles from the `Enzo` run were used to determine the initial conditions. That is, the dark matter particles were set identical to those in the `Enzo` run and baryons were added based on the dark matter distribution (no separate transfer function). We expect these differences to be negligible by the redshift where galaxies are forming.

Based on the cosmological model specified above, all Lagrangian codes set the gas mass resolution ($m_{\rm gas} = 3.3 \times 10^4 M_\odot$) relative to the dark matter particle mass ($m_{\rm DM} = 1.75 \times 10^5 M_\odot$). Table 1 outlines many of the pertinent details for each code, including star formation (SF) density thresholds and efficiency parameters, epoch of reionization, UV background model, and the type of stellar feedback model adopted. Below, we describe the gas cooling and feedback physics of each individual runs in more detail and include references to recently published science papers that utilize similar subgrid physics models as those implemented here.

For all analysis that follows, we make the distinction between "cold" and "hot" gas by a temperature cutoff of 250,000 K (commonly used as the distinction between "cold–mode" and "hot–mode" gas accretion, e.g., Kereš et al. 2005, 2009; Stewart et al. 2011b, 2013). For the sake of uniform comparison between codes we choose a fiducial value of 300 comoving kpc as an approximation of the virial radius at each epoch, due to the fact that halo–finding algorithms produce slightly different virial radii at the same epoch for different simulations (varying within the range of $\sim$ 280–320 comoving kpc for $z < 3$). In order to guarantee uniform analysis for the varied code architectures and file formats, all analysis presented here has been performed utilizing the `yt`[16] analysis software (Turk et al. 2011; Turk & Smith 2011; Turk 2013), an open source project which has been developed and is continually being maintained and improved by the astrophysical community for the intended purpose of supporting cross–code compatible hydrodynamic analysis routines.

2.2. *Enzo*

The `Enzo` (Bryan et al. 2014) run serves as the basis for the Scylla simulation suite, and was performed in 2010 by Ryan Joung and discussed in Joung et al. (2012); Fernández et al. (2012); and Putman et al. (2012). `Enzo` uses an Adaptive Mesh Refinement (AMR) grid to solve the equations of hydrodynamics, with this particular run using a version of `Enzo` before the uniform release of `Enzo` 2.0. `Enzo` uses an FFT in the root grid gravity

[15] http://web.mit.edu/edbert/

[16] http://yt-project.org

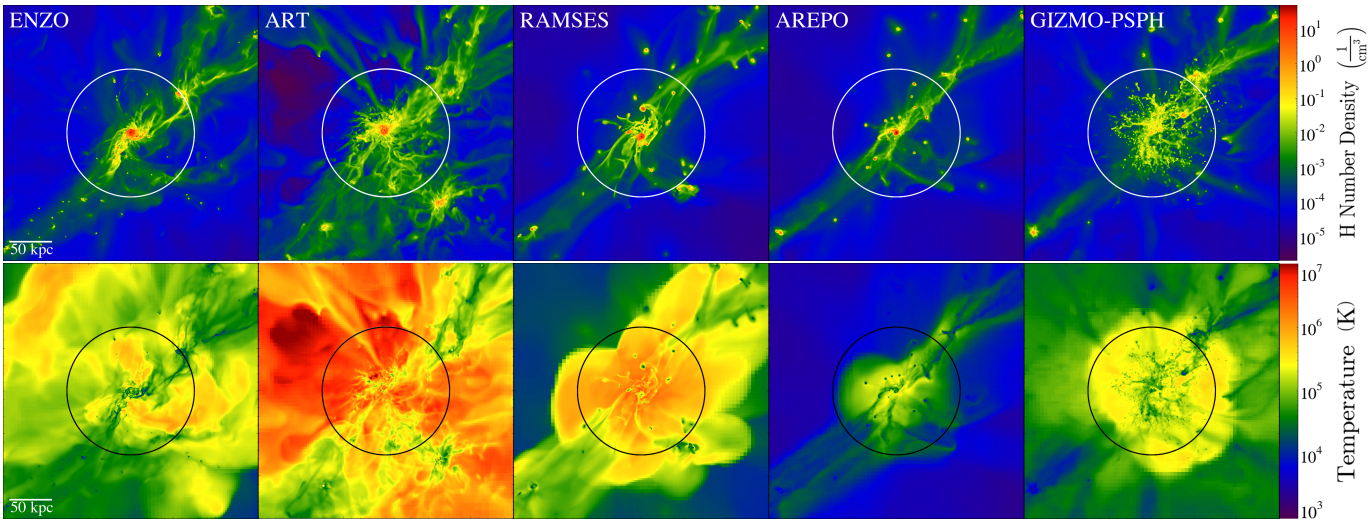

Figure 1. Hydrogen number density and temperature comparison at $z = 3$. All panels show the circumgalactic region, with panel widths of 300 physical kpc. Physical size scales are given in the left–most panels, and circles denote a radius of 300 comoving kpc (75 physical kpc), which is roughly the virial radius of the halo. *Top:* Projected gas density, showing the gas accretion onto the galaxy via cosmic filaments. Detailed morphology of the resulting galaxy varies between simulation codes, but the same filamentary accretion structure is apparent. *Bottom:* Projected density–weighted gas temperature. Note that temperature of gas in the CGM is highly dependent on the specific feedback and code implementation.

solver and a 3rd order piecewise parabolic method hydrodynamics solver. Feedback is thermal as described in Cen et al. (2005). The simulation includes metallicity–dependent cooling to a temperature of 10 K (Dalgarno & McCray 1972), neutral hydrogen shielding from UV radiation, and diffuse photoelectric heating (Abbott 1982; Joung et al. 2009).

2.3. *Art*

The `Art` (Kravtsov et al. 1997; Kravtsov 2003) run uses an AMR grid to solve the equations of hydrodynamics. `Art` uses a multilevel particle mesh gravity solver and a 2nd order Godunov method hydrodynamics solver. Our run uses the star formation and feedback models described in Ceverino et al. (2014) and includes thermal feedback from supernovae explosions and stellar winds (Ceverino & Klypin 2009; Ceverino et al. 2010) as well as radiative feedback (model *RadPre_LS_IR* in Ceverino et al. 2014). This model of radiative feedback includes radiation pressure from ionizing and infrared photons, photoheating, and photoionization from massive stars. Other recent papers using similar physics include Zolotov et al. (2015); Snyder et al. (2015a); Ceverino et al. (2015); Goerdt & Ceverino (2015); Mandelker et al. (2015); Tacchella et al. (2016b,a); Ceverino et al. (2016, 2015) and Tomassetti et al. (2016).

2.4. *Ramses*

The `Ramses` (Teyssier 2002) run (`Ramses` version 3.0) uses an AMR grid to solve the equations of hydrodynamics. `Ramses` uses a particle mesh gravity solver and a 2nd order MUSCL sheme hydrodynamics solver. The gas cooling is based on a metallicity–dependent cooling, including metal line cooling down to a temperature floor of 100 K. A stiffening of the interstellar medium (ISM) equation of state (chosen as a power law with $\gamma = 4/3$) was used to prevent gas with densities higher than the 1 atom/cm^{-3} threshold to cool further than 100 K and artificially fragment. Feedback includes energy from stellar winds and supernovae (deposited in kinetic form) following Dubois & Teyssier (2008), where the proper distributions of type II supernova lifetimes are based on Leitherer et al. (1999) and Leitherer et al. (2010), such that energy from type II supernovae is injected continuously between 2 and 50 Myr. Feedback from type Ia Supernovae are also included, following Greggio & Renzini (1983) to compute the SN frequency. This run has essentially the same physics as in Dubois et al. (2014); Welker et al. (2014); Codis et al. (2015); and Chisari et al. (2015) with the exception that we have not included any AGN physics here.

2.5. *Arepo*

The Arepo (Springel 2010) run employs a quasi–Lagrangian finite volume method for solving the hydrodynamic equations of motion (Vogelsberger et al. 2013). The version of `Arepo` used here employs a tree multipole expansion gravity solver and a 2nd order Godunov method hydrodynamics solver with a MUSCL scheme, however subsequent versions of Arepo have switched to a different time integration in the hydrodynamics solver (Pakmor et al. 2016) using Heuns method. Radiative gas cooling includes both primordial cooling (Katz et al. 1996) as well as line cooling from heavy elements (Wiersma et al. 2009a; Vogelsberger et al. 2013). Pressurization of the ISM, star formation, and associated feedback is handled using the Springel & Hernquist (2003) subgrid model. Time delayed stellar mass return and metal enrichment is carried out (Wiersma et al. 2009b; Vogelsberger et al. 2013), and kinetic star formation driven winds are employed with a wind velocity scaled to the local dark matter velocity dispersion. Winds are launched carrying 40% of the local ISM metallicity to prevent over ejecting metal mass from the dense ISM (Zahid et al. 2014).

This run includes a physics implementation that is similar to that used in the `Illustris` simulation (Vogelsberger et al. 2014; Genel et al. 2014) with the notable difference that no AGN physics is included here. Other recent work that contains similar physics include Tor-

rey et al. (2014); Wellons et al. (2015b,a); Torrey et al. (2015b,a); Snyder et al. (2015b); Rodriguez-Gomez et al. (2015); Sales et al. (2015); Bray et al. (2015); and Mistani et al. (2015).

2.6. *Gizmo–PSPH*

The `Gizmo-PSPH` (Hopkins 2015) run uses a tree multipole expansion for the gravity solver and the pressure–energy formulation of smoothed particle hydrodynamics (PSPH; Hopkins 2013) together with a number of additional improvements to artificial viscosity, timestepping, and higher–order kernels, to solve the equations of hydrodynamics.[17] Radiative gas cooling includes both primordial cooling (Katz et al. 1996) as well as cooling from 11 separately tracked metal species (Wiersma et al. 2009a). Gas follows an ionied + atomic + molecular cooling curve from $T = 10 - 10^{10}$ K.

Star formation and feedback uses the *Feedback In Realistic Environments* (FIRE) prescriptions from Hopkins et al. (2014), which explicitly follow the mass, metal, momentum, and energy deposition by radiation pressure, photo-ionization and photo–electric heating, stellar winds, and SNe (Types II and Ia), with all rates tabulated from the stellar population model STARBURST99 (Leitherer et al. 1999) assuming a Kroupa (2001) IMF. They do not include AGN feedback. Unike the other codes here, which assume stars form with a relatively low efficiency per free–fall time in all gas above some relatively large density threshold $\sim 0.1-1$ cm^{-3}, the FIRE models restrict star formation *only* to gas which is locally self–gravitating (following Hopkins et al. 2013), self–shielding and molecular (following Krumholz & Gnedin 2011), Jeans–unstable, and exceeds a higher density $n > 5$ cm^{-3}, but within this highly restricted gas assumes the star formation occurs on a free–fall time. The FIRE code and methods are identical in this paper and in all published papers including e.g. Oñorbe et al. (2015); Chan et al. (2015); Ma et al. (2015); Faucher-Giguère et al. (2015); Wheeler et al. (2015) and others.

3. BASIC HALO PROPERTIES

3.1. *Large Scale Structure and Mass Growth*

We begin with a visual inspection of the region around the galaxy for each simulation. Figure 1 shows the gas density (number density of H; top) and density-weighted temperature (bottom) projections at $z = 3$ through a cube of width 300 physical kpc ($\sim 4R_{\rm vir}$ at this redshift). The top panels of Figure 1 show qualitative agreement between the simulations on the general geometry and structure of the forming disk galaxy at this redshift, as well as its placement in a large-scale cosmic filament that is continually delivering an inflow of cold gas into the virial radius of the galaxy. However, the detailed structure of the galaxy—and even that of the filament into which the galaxy is embedded—does appear to vary significantly between simulations. For example, the width of the cosmic filament, the size and structure of the galactic disk, and the peak density of infalling satellite galaxies all vary on a noticeable level.

[17] `Gizmo` is a multi–methods code which gives the user the choice of several hydrodynamic methods. This is why we use the label `Gizmo-PSPH` throughout this work, to distinguish the PSPH implementation from alternate methods.

Perhaps more striking is the temperature differences among simulations shown in the bottom panels of Figure 1. All simulations demonstrate the presence of a significant gaseous halo around the galaxy, as well as streams of filamentary gas that penetrate the halo and deposit cold gas in the inner halo, near the galactic region. However, the extent that feedback has enriched the CGM and IGM, the density structure of the gaseous halo, the temperature distribution of hot gas, and the precise structure of the cold flows as they interact with the gaseous halo of the galaxy vary significantly among simulations.

To illustrate some of the similarities and differences among the simulations, Figure 2 shows the mass growth of the halo as a function of time—including the total mass (black), total gas mass within the virial radius (cyan), total stellar mass within the virial radius (yellow) and the total hot ($T > 250,000$ K) gas mass within the virial radius (magenta). Note that the total virial mass and the total gas mass are both quite robust among simulations—despite very different feedback implementations. However, the total stellar mass and the total mass in hot gas varies significantly among some simulations. (Alternatively, the total mass in cold gas also differs significantly among simulations, however for the sake of clarity cold gas masses are not shown in the figure).

We note that the `Gizmo-PSPH` code shows a significantly lower stellar masss than any of the other codes used here, likely as a result of strong feedback implementations. Interestingly, the galaxy stellar mass for `Gizmo-PSPH` is much closer to observational expectations—for example, abundance matching suggests that a $10^{12} M_\odot$ halo at $z = 1$ should host a central galaxy with a stellar mass of $\sim 2\times10^{10} M_\odot$ (Behroozi et al. 2010). As our goal in this work is to focus on *similarities* between codes, with emphasis on the galaxy halos and not the galaxies themselves, we defer a more detailed discussion of the numerous differences between the simulations and their implications for galaxy formation as a topic for future study.

3.2. *Angular Momentum*

One fundamental result of the recent emerging picture of angular momentum acquisition in galaxies is that gas in the halos of galaxies tends to have specific angular momentum $\sim 3-5$ times higher than the dark matter (Stewart et al. 2011b; Kimm et al. 2011; Stewart et al. 2013; Danovich et al. 2015). We revisit these previous findings by comparing the spin parameter, λ, of both the cold halo gas and the dark matter in the halo for all our simulations. We adopt the spin parameter from Bullock et al. (2001): $\lambda_x \equiv j_x/\sqrt{2}VR$, where λ_x is the spin parameter of a given component, based on that component's specific angular momentum, j_x, and V and R are typically defined by the virial velocity and virial radius of the halo, respectively. However, in order to make a uniform comparison between simulations, we approximate the halo virial radius by $R = 300$ comving kpc, where V is then defined by the circular velocity at this radius, $\sqrt{GM/R}$. Figure 3 shows the spin parameter for each saved output of each simulation between $z = 3$ to $z = 1$, where we only include material inside the virial radius but outside of the central region, $R > 0.1R_{\rm vir}$, in

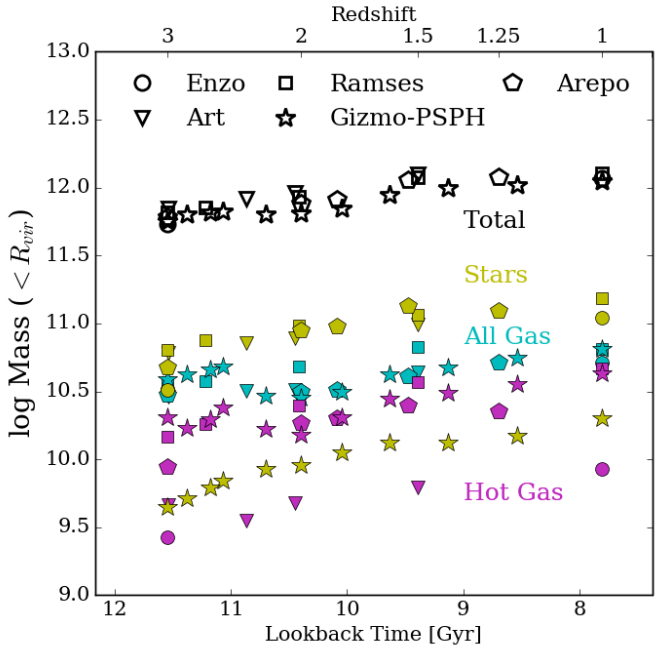

Figure 2. Masses enclosed within 300 comoving kpc (roughly the virial radius) as a function of time. Note that the total virial mass and total gas masses are similar. However, the total stellar mass and the total *hot* gas in the halo (or total cold gas—not shown for the sake of clarity) may vary significantly depending on which code and feedback implementations are used.

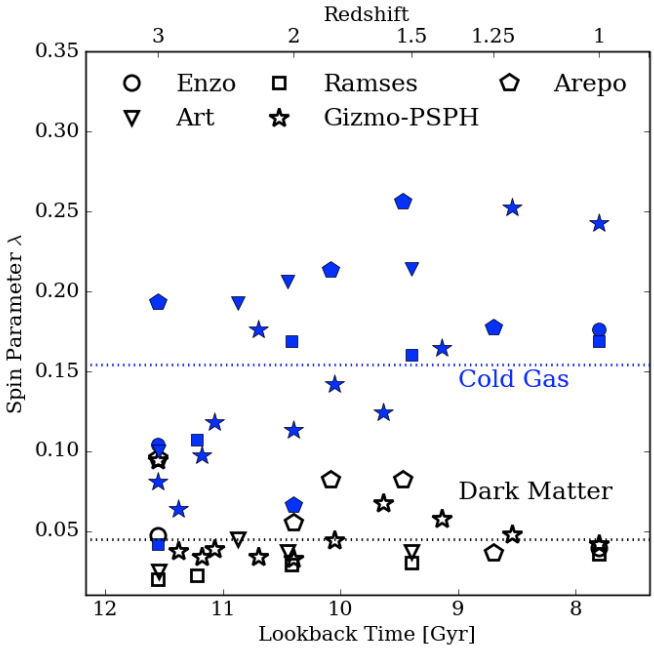

Figure 3. Spin parameter of cold halo gas and dark matter inside the galaxy halo (but excluding material within $R < 0.1R_{\rm vir}$ so as not to include the galaxy) from $z = 3$—1. Different symbols represent outputs from different simulations, and the mean values across all simulations for the cold halo gas and dark matter are given by the blue and black horizontal dotted lines, respectively. All simulations demonstrate that cold halo gas has significantly higher spin parameter compared to the dark matter, with typical values of $\lambda_{\rm cold} \simeq 0.15$.

our calculations (after all, were are interested in the *halo*, not the galaxy itself). While the simulations vary in the precise value (and direction—not shown) of the angular momentum of their gaseous halos, we find several important qualitative agreements across all the simulations.

- Both cold halo gas (and hot halo gas—not shown in the figure, for clarity) consistently have more specific angular momentum than the dark matter component.
- While simulations agree that dark matter halo spin parameters are typically $\lambda_{\rm DM} \simeq 0.04$, the average cold halo gas spin parameter across our simulations is $\lambda_{\rm cold} \simeq 0.15$.
- In agreement with previous work, in all simulations the cold halo gas contain $\simeq 4$ times the specific angular momentum of the dark matter halo (though with considerable variation), while the hot gas typically has $\simeq 2$ times the specific angular momentum of the dark matter.

These findings confirm previous results: the angular momentum of galaxy halos varies significantly among components; the dark matter invariably measures a cumulative combination of past accretion, resulting in the lowest specific angular momentum; the hot gaseous halo is typically built and maintained both by non-filamentary "hot-mode" gas accretion, as well as feedback and outflows (which are sensitive to subgrid physics models); and the cold halo gas traces filamentary "cold-mode" accretion and has the highest specific angular momentum. Thus, while our simulations agree with previous N-body simulations for a dark matter halo spin parameter of $\lambda_{\rm DM} \simeq 0.04$, one should expect to observe typical cold halo gas with significantly higher angular momentum, with spin parameters closer to $\lambda_{\rm cold} \simeq 0.15$.

In a previous study of four cosmological zoom–in simulations (all using the same hydrodynamic code) Stewart et al. (2013) found no significant trend between cold gas spin parameter and cosmological time (or redshift). Therefore, while Figure 3 arguably shows a trend of increasing cold gas spin parameter from $z = 3 - 1$, this is likely a consequence of this particular halo's unique merger and accretion history, and not general result of galaxy formation in LCDM.

4. LARGE SCALE FILAMENTARY INFLOW

In order to place this high angular momentum cold halo gas in the proper cosmological context, Figure 4 shows the large–scale environment around the simulated galaxy—where, for purposes of this work, we define the halo environment by box widths of 2400 comoving kpc (300 physical kpc at $z = 3$). The top panels again show the gas density (H number density), similar to Figure 1 but zoomed out by a factor of two and viewed along an orthogonal orientation. The bottom panels show the line of sight velocity of all cold gas above a minimum density threshold in hydrogen (all forms) of $n_{\rm H} > 3\times10^{-4}$ cm^{-3}, which was chosen to select only gas sufficiently dense to be embedded in filamentary (or dark matter halo) structures on these large scale environments.

Because the galaxy is the most massive halo in its environment (i.e. not a member of a group or cluster) the cosmic filaments in its environment are strongly af-

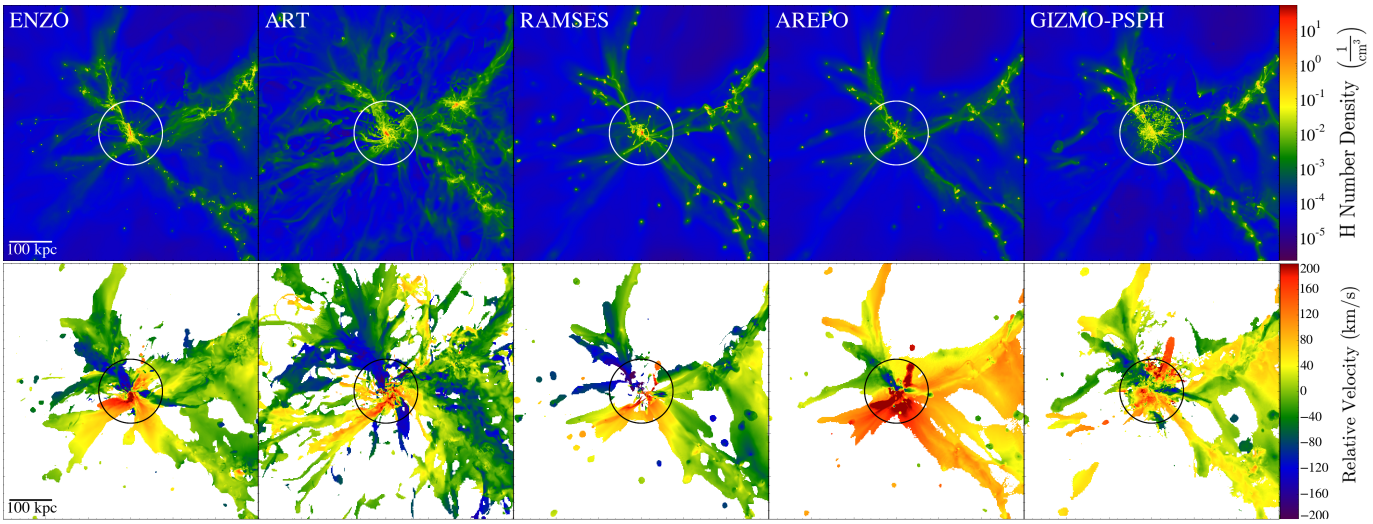

Figure 4. Large scale environment at $z = 3$ (along an orthogonal line of sight from Figure 1). In all panels, circles denote 300 comoving kpc (roughly the virial radius of the halo) and the size scale in physical kpc is indicated in the left–most panels, with panel widths of 600 physical kpc. *Top:* Gas density projections showing the structure of the cosmic web near the galaxy. *Bot:* Line of sight velocity of dense cold gas with a density in hydrogen of $n_{\rm H} > 3 \times 10^{-4}$ cm^{-3} in an identical orientation and scale as the top panels. There is a clear line of sight velocity signature—the top left filament is blueshifted while bottom filaments are redshifted—indicating the motion of the cosmic web as it flows onto the massive galaxy halo. The particularly chaotic structure of the `Gizmo-PSPH` simulation is due to a violent merger–induced outflow at this epoch; see §5.1.

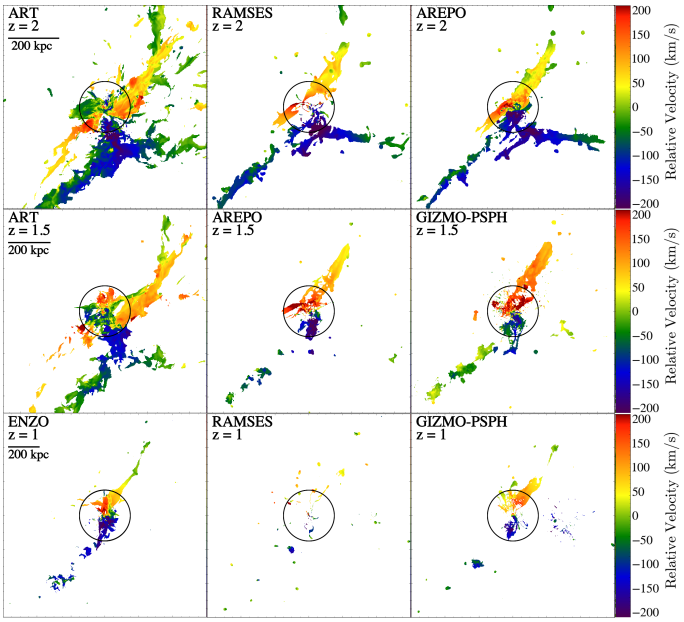

Figure 5. Large scale environments at $z = 2$ (top), $z = 1.5$ (middle) and $z = 1$ (bottom) for various subsets of the simulation runs. As with figure 4, the panels show the line of sight velocities of dense gas with hydrogen density of $n_{\rm H} > 3 \times 10^{-4}$ cm^{-3}. Each box has a width of 2400 comoving kpc across $(800, 960, 1200$ physical kpc at $z = 2, 1.5, 1$, respectively). Circles denote a 300 comoving kpc radius (roughly the virial radius of the halo) and the size scale in physical kpc is indicated in the left–most panels of each row. Again note the clear signature of large scale filamentary gas flowing onto the galaxy.

fected by the halo potential, with gas, dark matter, and smaller galaxies all flowing along the filaments towards the galaxy, demonstrated by the clear line of sight velocity indications in the bottom panels. For example, the filament to the upper–left of the galaxy (situated *behind* the galaxy along this line of sight) consistently shows blueshifted velocities in all simulations, while the two filaments below (and in front of) the galaxy are consistently redshifted.

This result is perhaps not surprising, as any three–dimensional filamentary structure where matter flows along the cosmic web towards a central overdensity (and is viewed along an arbitrary axis) is unlikely to show multiple filaments all flowing perpendicular to the line of sight. Thus one should naively expect strong line of sight velocities to be apparent when viewing large–scale filamentary gas flows. While this may not be a *surprising* result, however, it is important to keep these large scale gas flows in mind for future discussion of the origin of cold flow disks. We will see in §5 that these large–scale filamentary flows have a direct impact on the behavior of the cold gas within the virial radius of the halo.

Note that the line of sight velocity structure of the filament flowing in from the *right* of the galaxy shows considerably more variation between the simulations. This occurs because this filament *does* happen to be roughly perpendicular to the line of sight. Thus the velocities along the right–most filament are more sensitive to the peculiar velocities of galaxies, gas streams, and outflows, which vary more strongly between simulations than the gross large–scale flows towards the central halo.

Figure 5 show line of sight velocity maps along an orthogonal orientation for dense cold gas at $z = 2$ (top), $z = 1.5$ (middle) and $z = 1$ (bottom) for various subsets of the simulation runs (as labeled). While the basic filamentary nature of the gaseous inflows becomes less apparent at decreasing redshift (when the filaments are less dense), we can still note the same qualitative behavior of inflowing gas. On environmental scales, filamentary inflow results in the same clear line of sight velocity signature as before; across all simulations, gas flowing into the virial radius from the top of the panels is redshifted, while gas flowing in from the bottom is blueshifted. The only notable exception is the `Ramses` code at $z = 1$, which is likely the result of the lack of self–shielding from the UV background leaving very little cold gas above our minimum density threshold, so almost no cold dense inflow

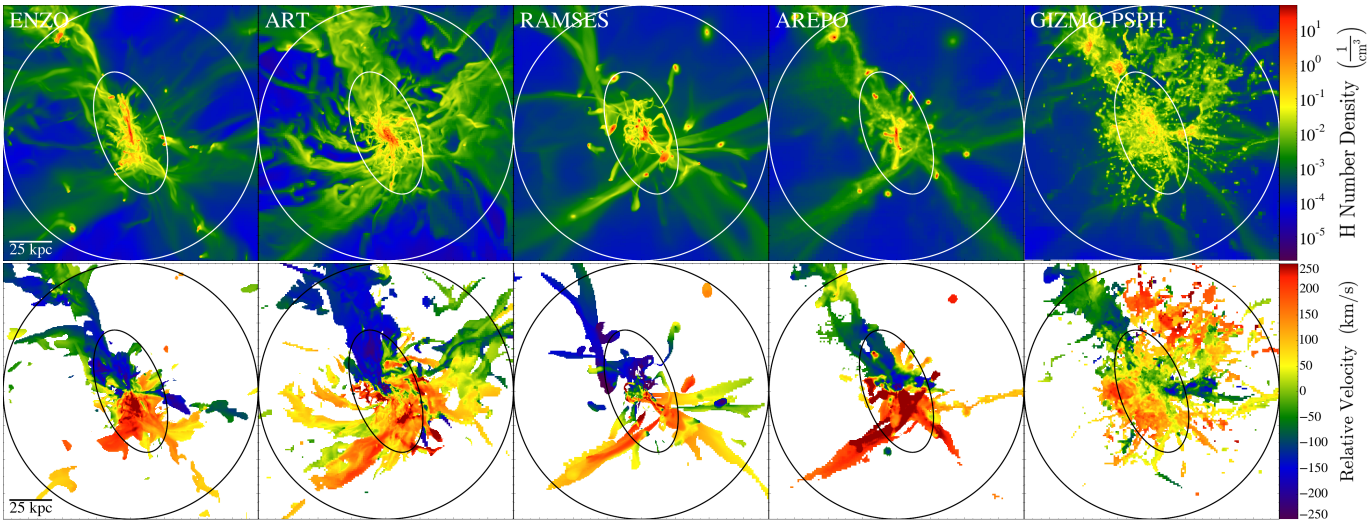

Figure 6. Density projections and line of sight velocities at $z = 3$, similar to figure 4 except that panels have now been "zoomed in" to widths of 150 physical kpc, and the minimum density threshold for hydrogen gas in the bottom panels has been increased by a factor of 10 from Figure 4 to a hydrogen density of $n_{\rm H} > 3 \times 10^{-3}$ cm^{-3} (corresponding to column densities of $N_{\rm HI} \gtrsim 10^{17}$ cm^{-2}). Circles denote 300 comoving kpc (roughly the virial radius of the halo) and the size scale in physical kpc is indicated in the left–most panels. In all simulations, the high angular momentum cold filamentary gas accretion results in cold flow disks—large rotating disk–like structure of cold dense gas in the galaxy halo that are kinematically linked to the large–scale filaments that are fueling them (see the similar line of sight velocities of the inflowing filaments in Figure 4). The overlaid ellipse in each panel roughly corresponds to this "cold flow disk" region, to aid the eye in comparison between images. The particularly chaotic structure of the `Gizmo-PSPH` simulation is due to a violent merger–induced outflow at this epoch; see §5.1.

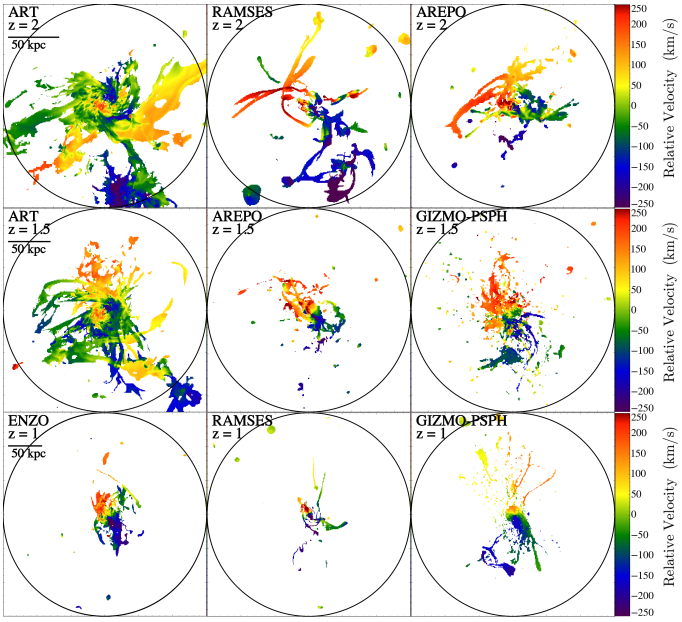

Figure 7. Line of sight velocities at $z = 2$ (top), $z = 1.5$ (middle), and $z = 1$ (bottom) for various subsets of the simulation runs, similar to bottom panels of Figure 6. Each box has a width of 600 comoving kpc across (200, 240, 300 physical kpc at $z = 2, 1.5, 1$, respectively). Circles denote 300 comoving kpc (roughly the virial radius of the halo) and the size scale in physical kpc is indicated in the left–most panels of each row. In all simulations, cold flow disks seem to be a common, though not ubiquitous, result of high angular momentum, filamentary accretion of cold gas into the halo.

is still visible in the figure. While the detailed structure of the inflowing gas again varies among simulations, it seems apparent that filamentary gas accretion along a three–dimensional cosmic web onto an overdense region (at this mass scale from $1 < z < 3$) tends to produce the same qualitative picture across all the simulations, regardless of subgrid physics.

5. COLD FLOW DISKS

As shown in previous work (Stewart et al. 2011b, 2013; Danovich et al. 2015), a natural consequence of high angular momentum inflow of cold filamentary gas is the existence of cold flow disks—extended, flattened rotating structures of high–angular momentum material, aligned and fueled by filamentary inflow. We now investigate the robustness of these previous results using our suite of simulations. Figure 6 is analogous to Figure 4, except that the panels now focus on material within the virial radius (panel widths of 150 physical kpc at $z = 3$). The bottom panels again show line of sight velocity maps of cold dense gas[18] in the halo, except that we have increased the minimum density threshold by a factor of 10 when compared to Figure 4, to a hydrogen density of $n_{\rm H} > 3 \times 10^{-3}$ cm^{-3} (this should correspond to a minimum hydrogen column density of $N_{\rm HI} \gtrsim 10^{17}$ cm^{-2}, Altay et al. 2011; Schaye 2001).

The exact morphology of gas in the halo of the galaxy varies considerably between the simulations, not surprisingly, given the vastly different feedback mechanisms implemented in each simulation—some of which drive explosive spherical outflows that violently shred the ISM and CGM of the galaxy (e.g., `Gizmo-PSPH`) and some of which instead drive high–velocity bi-conical outflows out of the plane of the galaxy (e.g., `Enzo`). However, we also note that some of the morphological differences are also influenced by the precise timing of galaxy mergers. For example the `Gizmo-PSPH` simulation is in the

[18] We select gas based on temperature and density rather than H I content or species column density because we want to avoid any differences in ionization fractions among simulations when making our comparison. The qualitative trend that there is always orbiting "cold flow disk" gas in the halo does not depend on the details of this selection criterion, though quantitative measures (e.g., the apparent covering fraction of this gas) will of course depend on these details—a topic we plan to revisit in future work.

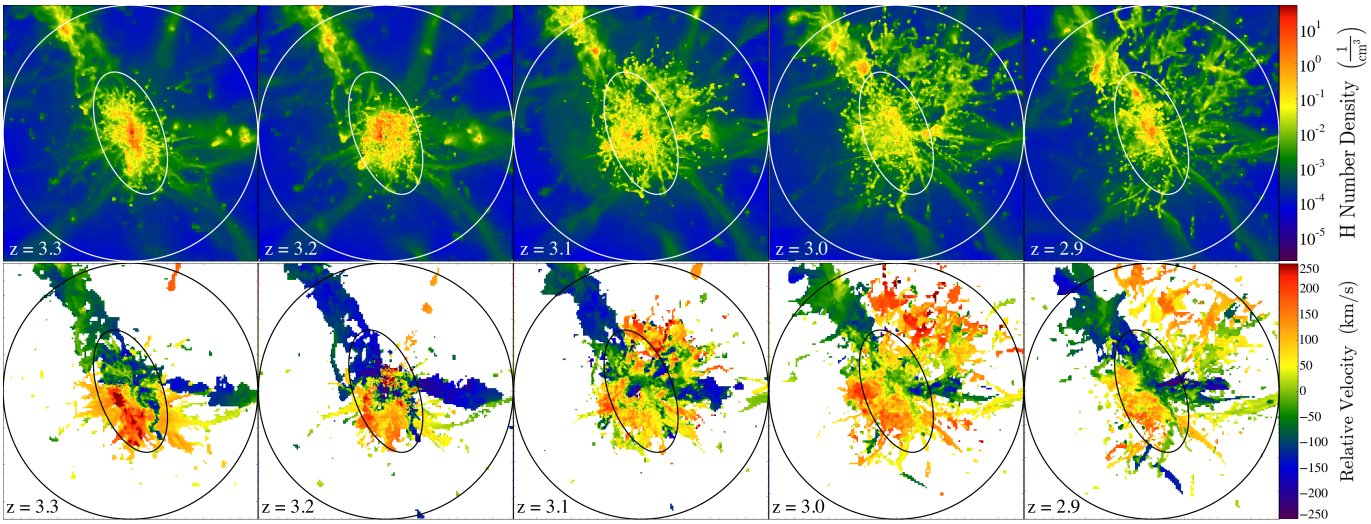

Figure 8. Time lapse of a post–merger violent outflow event in `Gizmo-PSPH` at $z \sim 3$, proceeding from left–to–right. The overlaid circles denote 300 ckpc, roughly the halo virial radius and the overlaid ellipse in each panel roughly corresponds to the "cold flow disk" region, to aid the eye in comparison between images. *Top:* density map of the gas in the halo. *Bottom:* line of sight velocity of cold dense gas in the halo (identical analysis to Figure 6). The cold flow disk apparent in the left panel by the coherent rotation in the bottom–left panel is effectively destroyed by the violent outflow from $z = 3.2$—3.0, but once the outflow event is over, fresh high angular momentum infall along the cosmic web begins to establish a new cold flow disk by $z = 2.9$, demonstrating the robustness of the cold flow disk phenomenon.

midst of a violent outflow at this epoch, due to a recent major merger, which partially explains the chaotic structure shown in Figure 6 (We will demonstrate in §5.1 that the `Gizmo-PSPH` simulation shows the presence of a cold flow disk immediately before *and after* this merger–driven outflow event). While the same general merger and accretion history takes place for each simulation, the exact timing of these mergers at a given epoch may vary, and any coherent velocity structure for cold gas in the galaxy's halo is typically destroyed during a sufficiently strong outflow event.[19]

Despite these varied differences in morphology, the bottom panels of Figure 6 show a remarkably similar qualitative picture. As was the case with the large scale environment, the cold gas entering the virial radius from the upper–left filament shows a dramatic blueshift in each simulation, while the cold gas entering from the bottom filaments show dramatic redshifts. (As before, the line of sight velocity of the material in the upper–right quadrant of these panels is less uniform, as it probes a gas accreting along a filament that is roughly perpendicular to the line of sight.) The qualitative result in each case is a massive clumpy and chaotic disk–like structure of co–planar high angular momentum cold gas accretion kinematically linked to inflow from the cosmic web—i.e., what has been previously referred to as a "cold flow disk." To aid the eye in comparing the images, an ellipse has been overlaid on each image roughly corresponding to this cold flow disk region, inside of which coherent rotation of inflowing cold gas is apparent). Though the precise extent, orientation, clumpiness, size, and structure of these disks vary between simulations, each code produces a qualitatively similar picture, where there is a clear rotational velocity structure within the virial radius of the halo that is kinematically linked to that of the large–scale filamentary environment of Figure 4 (with the exception of the `Gizmo-PSPH` simulation at this epoch; see §5.1).

We repeat a similar line of sight analysis along an orthogonal orientation within the halo virial radius for $z = 2$ (top), $z = 1.5$ (middle) and $z = 1$ (bottom) for various subsets of the simulation runs in Figure 7. Again, the precise structure of these disks varies between simulations, but most of the simulations produce qualitatively similar pictures; there is a clear rotational velocity structure within the virial radius of the halo that is kinematically linked to the large–scale filamentary inflow shown in Figure 5). As with Figure 5, the only exception appears to be `Ramses` at $z = 1$, which has evacuated most of its halo of cold dense gas altogether, likely as a result of the lack of UV self–shielding implementation in the simulation. These qualitatively similar results, across a broad range in hydrodynamic code types and subgrid physics models of galaxy formation, seem to suggest that the formation of cold flow disks at $z > 1$ is a natural consequence of high angular momentum filamentary inflow along the cosmic web, and represents a robust prediction of cosmological gas accretion in LCDM.

5.1. *The rapid destruction and reformation of a cold flow disk at $z = 3$*

In the discussion of Figures 4 and 6, we noted that the velocity structure of the galaxy in the `Gizmo-PSPH` simulation is not nearly as clean and orderly as the other simulations at $z = 3$, and therefore does not seem to host a clear cold flow disk structure. While we thought it important to show all galaxies at precisely the same epoch, we note that in `Gizmo-PSPH`, the galaxy happens to be in the midst of a post–merger starburst, accompanied with a violent outflow event at this epoch, due to this code's strong feedback physics. Halo–halo mergers, of course, tend to occur at broadly similar times in all codes, but differences in galaxy masses and halo baryonic mass distributions mean that the galaxy–galaxy mergers can and do occur at significantly different times, and with different mass ratios and corresponding consequences for star formation, at the halo center (see e.g. Stewart et al.

[19] As another example of different merger timing, note the location and structure of the infalling galaxy embedded in the filament to the upper–left of the main galaxy in each panel.

2009; Hopkins 2010). The obvious clumpiness of the outflows may owe, at least partially, to well–known numerical difficulties capturing fluid–mixing instabilities in SPH, even in the improved P–SPH implementation; this is supported by early results from the FIRE–2 simulations, which use a different, mesh–free Godunov–type finite volume method to solve the hydrodynamics (P. Hopkins, private communication).

In Figure 8, we show the structure of this galaxy immediately before and after this violent merger event. The time sequence begins in the left panel at $z = 3.3$, where inflowing cold gas demonstrates coherent rotation in the galaxy halo, including a large cold flow disk of accreting gas. (To aid the eye in comparing the images, some of which are quite chaotic during the outflow, an ellipse has been overlaid on each image roughly corresponding to this initial cold flow disk region—identical to those in Figure 6.) At this epoch, the recent influx of of fresh gas onto the central regions of the galaxy results in a spike in star formation, and consequently a violent spherical outflow event from $z = 3.2$—3.0 that effectively destroys the ISM of the galaxy (leaving a deficit of gas in the center of the galaxy, as seen at $z = 3.1$) and disrupting the inflowing filamentary gas in the CGM of the halo. However, the filamentary gas continues to flow into the halo, and this inflow continues to contribute substantial angular momentum. As a result, a new cold flow disk begins to form almost immediately after the outflow event has subsided, again showing orderly rotation of fresh gas inflow along a very similar orientation to the original cold flow disk (right–most panel). We argue that the bursty nature (Muratov et al. 2015) of the subgrid physics as implemented in `Gizmo-PSPH` coupled with this demonstration of the near–immediate regrowth of a cold flow disk after a massive outflow event only reinforces the robust nature of cold flow disk formation in LCDM.

6. DISCUSSION

Our results indicate that the existence of the cold flow disk phenomenon is expected to be a robust prediction of LCDM that is not sensitive to variations in current subgrid physics models or hydrodynamic astrophysical code implementations. This finding has significant implications for the observational verification of the cold flow scenario (as discussed in the Introduction). While the cold flow paradigm of gas accretion and galaxy formation has been increasingly emphasized in galaxy formation theory, it is quite difficult to observationally verify this mode of gas accretion onto galaxies. Extended, high–angular momentum, co–rotating gaseous structures are a testable observational signature of the cold flow model of galaxy formation.

Encouragingly, there is a growing body of observational evidence that seems to indicate that co–rotating halo gas of this kind is present around real galaxies. For example, kinematic studies of some Ly-α nebulae suggest rotational velocities and inflow rates consistent with those expected for cold flow disks (Martin et al. 2014; Prescott et al. 2015). Similarly, absorption line studies are beginning to emphasize the bimodal distribution of absorption detections, where detections along the galaxy's minor axis tend to show absorption properties consistent with outflowing gas, while detections roughly along the galaxy's major axis demonstrate properties (such as co-rotational inflow) that are consistent with cold flow disks (Kacprzak et al. 2010, 2012a,b; Bouché et al. 2012, 2013; Crighton et al. 2013; Nielsen et al. 2015; Bouché et al. 2016)

In perhaps the most direct confirmation of the existence of cold flow disks, Martin et al. (2015) performed a spectroscopic analysis on the cosmic filament (illuminated by two nearby QSOs) first detected by Cantalupo et al. (2014) at $z \sim 2$, and found that a substantial fraction of what was initially thought to be part of the illuminated filament was in fact a massive rotating gaseous structure. This extremely extended gaseous disk (extending to $\sim R_{\rm vir}/2$, corresponding to a width of 125 physical kpc) showed smooth rotation kinematics, with one side of the disk kinematically linked to the inflow velocity of the nearby cosmic filament. This very closely resembles what we have presented here for cold flow disks, though we note that the particular system observed by Martin et al. (2015) was estimated to be a much more massive halo than what we have simulated here ($M_{\rm vir} \sim 10^{13} M_{\odot}$) and it therefore had a correspondingly more massive cold flow disk than show here, as might be expected for a larger, more massive halo. A similar cold flow protodisk, again fed by a cosmic filament that was first detected in Ly-α emission, was also reported in Martin et al. (2016), suggesting that cold flow disks may be common phenomena for massive galaxies at high redshift.

While not seen in our particular simulations, we also speculate that polar ring galaxies—which have previously been suggested as evidence of cold flow gas accretion onto galaxies (Macciò et al. 2006; Brook et al. 2008; Spavone et al. 2010)—may be a result of a similar phenomenon. Such galaxies could reasonably occur when strong central torques (e.g., from a major galaxy merger) result in a near perpendicular misalignment between the angular momentum of the central galaxy and that of the inflowing cold mode gas.

We note that the cold flow disks in our simulations are significantly more massive and extended (relative to the halo virial radius) at high redshift, when cosmic filaments are more narrowly defined and contain higher density gas flows. However, Figure 3 and previous work (e.g., Stewart et al. 2013) both demonstrate that accreting cold gas continues to have high angular momentum, even at later times where the rotational signature of a cold flow disk is less clear. We speculate that it may be possible that this high angular momentum accretion helps to explain observations of extended XUV disks (e.g. Thilker et al. 2005, 2007; Lemonias et al. 2011; Holwerda et al. 2012), local extended H I disks (e.g. García-Ruiz et al. 2002; Oosterloo et al. 2007; Walter et al. 2008; Christlein & Zaritsky 2008; Sancisi et al. 2008; Wang et al. 2013; Huang et al. 2014; Courtois et al. 2015) and co-rotating cold halo gas around local Milky Way analogs (e.g. Diamond-Stanic et al. 2015).

Indeed, these growing observations of high angular momentum material in the outskirts of galaxy halos would be quite difficult to explain if one were to assume the canonical picture of galaxy formation whereby baryons in galaxy halos share the same distribution of angular momentum as the dark matter. In contrast, the cold flow paradigm naturally predicts that halo gas (and particularly the cold halo gas) preferentially constitutes re-

cent gas accretion from the cosmic web, with $\sim$ 3—5 times the angular momentum of the dark matter, naturally explaining the kinds of high angular momentum phenomena being observed. We caution, however, that we have not focused on the gaseous halos in our simulations at $z < 1$ here, and leave a more detailed comparison between simulations and low–z observations as a topic of further study.

7. CONCLUSION

We have simulated the evolution of a Milky Way sized galaxy from identical cosmological initial conditions with a variety of simulation codes:, `Enzo`, `Art`, `Ramses`, `Arepo`, and `Gizmo-PSPH`. Each code has used subgrid physics models drawn from scientific literature common to each simulation type, and we have compared the simulations in an attempt to draw robust conclusions about galaxy formation in LCDM (focusing on $z > 1$) that are not sensitive to uncertain aspects of galaxy formation simulations. To ensure uniform analysis among the various code types, we have used the hydrodynamic analysis software `yt`, which enables the same analysis routine to be performed on each code.

While we found many aspects of the simulated galaxies that did vary substantially among the simulations (e.g. morphology, stellar mass, hot halo temperature and density, to be discussed further in future work), we found the following qualitative features *common to all simulations, regardless of which subgrid physics model or hydrodynamic code was used*:

1. Gas in the galaxy halo has substantially higher specific angular momentum than the dark matter in the halo, with mean values of $j_{\rm cold} \simeq 4 j_{\rm DM}$ and $j_{\rm hot} \simeq 2 j_{\rm DM}$ (though with considerable scatter), leading to a typical cold halo gas spin parameter of $\lambda_{\rm cold} \simeq 0.15$.

2. The large scale filamentary structure is qualitatively similar in all simulations (with minor variations, for example regarding lower mass streams of secondary importance to the galaxy's growth) The three–dimensional geometry of these filaments, which are all flowing towards the central galaxy (the highest overdensity in its environment) results in a strong line of sight velocity structure. Filaments flowing onto the galaxy from opposite directions (along an arbitrary line of sight) tend to show alternating blueshifted and redshifted velocities relative to the galaxy as they flow towards the galaxy center.

3. As the filamentary gas accretion enters the virial radius, the large scale velocity structure of the accreting filaments often leads to the creation of cold flow disks—massive gaseous disks of high angular momentum cold gas that is transitioning from the cosmic web, though the halo, to eventually accrete onto the galactic disk. This process is continuous and dynamic; even after violent outflow events disrupt the CGM, inflowing gas quickly regrows the cold flow disk soon after the outflow has subsided. The maximum line of sight velocity expected for these cold flow disks is $\sim$ 250 km/s (corresponding to roughly 1.5 times the virial velocity of the halo).

In this work, we have limited our analysis to the growth of a single Milky Way size halo at $z > 1$ using a variety of different hydrodynamic codes and feedback physics implementations. It is difficult to draw general conclusions about galaxy formation from the simulation of a single halo, however, a number of theoretical works have previously established the high angular momentum nature of filamentary gas accretion, using various hydrodynamic codes, larger cosmological volumes, and/or analysis of multiple zoom–in simulations. For example: Pichon et al. (2011) analyzed $\sim 15,000$ halos at $z > 1.5$ from a (lower resolution) cosmological–scale simulation using the `Ramses` code; in a companion work, Kimm et al. (2011) also included $\sim$ 900 intermediate resolution halos and 2 high resolution zoom–in simulations to $z = 0$ using `Ramses`; Stewart et al. (2011b, 2013) analyzed 4 zoom–in simulations to $z = 0$ using the SPH code `Gasoline`; and Danovich et al. (2015) analyzed 29 zoom–in simulations at $z > 1.5$ using the `Art` code. The results presented here demonstrate that the high angular momentum nature of cold gas accretion in LCDM is not likely to change (in the qualitative sense) among a broad range of different physics implementations and hydrodynamic codes, suggesting that high angular momentum halo gas (sometimes taking the form of cold flow disks) appears to be a robust expectation of LCDM.

We note that the *prevalence* of cold flow disks is yet to be fully understood, and thus cannot be determined from the single high resolution simulation presented here. The buildup of a cold flow disk is dependent on the geometry and kinematics of the cosmic web in the galaxy's environment, so we speculate that there are likely to be significant environment effects even at fixed halo mass. For example, Milky Way sized galaxies near the outskirts of galaxy clusters would not dominate the gravitational potential of the cosmic web in their large-scale environment, so we may not expect to find the same clear velocity signature of filamentary inflow (i.e., Figure 4) for such systems.

While all simulations presented here produced cold flow disks of a qualitatively similar nature at some point during the growth of the halo, we also note that there are considerable variations in their quantitative nature (morphology, rotational velocity, size, temperature, density, etc.). The exploration of the prevalence of cold flow disks in simulations, for different environments and halo masses, would be a useful topic of further study, especially in light of recent observations of a cold flow disks at $z \sim 2$ (Martin et al. 2015, 2016) that are strikingly similar to the qualitative results presented here.

Computations described in this work were performed using the publicly-available `Enzo` code (http://enzo-project.org), and the publicly-available `yt` toolkit (http://yt-project.org/), both of which are the products of collaborative efforts of many independent scientists from numerous institutions around the world. Their commitment to open science has helped make this work possible. KRS would especially like to thank Matt Turk and Nathan Goldbaum for their support with `yt`. KRS also thanks Volker Springel, Lars Hernquist and Paul

Torrey for running the Arepo simulation discussed in this work, for allowing us to include its results as part of this comparison project, and for providing useful discussions and comments.

KRS was supported by HST-GO-14268.026-A. JSB was supported by HST AR-12836. CAFG was supported by NSF grants AST-1412836 and AST-1517491, by NASA grant NNX15AB22G, and by STScI grants HST-AR-14293.001-A and HST-GO-14268.022-A. JD acknowledges support from the Spin(e) grant ANR-13-BS05-0005 of the French Agence Nationale de la Recherche (http://cosmicorigin.org). Support for PFH was provided by an Alfred P. Sloan Research Fellowship, NASA ATP Grant NNX14AH35G, and NSF Collaborative Research Grant #1411920 and CAREER grant #1455342. The Art run was performed at the National Energy Research Scientific Computing Center (NERSC) at Lawrence Berkeley National Laboratory. DC acknowledges support from the European Research Council under the European Communitys Seventh Framework Programme (FP7/2007-2013) via the ERC Advanced Grant STARLIGHT: Formation of the First Stars (project number 339177). The Ramses simulation was performed on the DiRAC Facility, jointly funded by BIS and STFC. JDs research is partly funded by Adrian Beecroft and the Oxford Martin School. The Gizmo-PSPH run was carried out on the CUNY HPC which is supported under National Science Foundation Grants CNS-0958379, CNS-0855217, ACI-1126113 and the City University of New York High Performance Computing Center at the College of Staten Island. Storage and analysis of the simulations was performed on the CTP cluster which is supported by GRTI grant CT04AGR15001 and Physics Division of the U.S. Army Research Office grant #64775-PH-REP.

REFERENCES

Abbott, D. C. 1982, ApJ, 263, 723
Agertz, O. & Kravtsov, A. V. 2015, ArXiv:1509.00853
Agertz, O., Kravtsov, A. V., Leitner, S. N., & Gnedin, N. Y. 2013, ApJ, 770, 25
Agertz, O., Teyssier, R., & Moore, B. 2009, MNRAS, 397, L64
Agertz et al. 2007, MNRAS, 380, 963
Altay, G., Theuns, T., Schaye, J., Crighton, N. H. M., & Dalla Vecchia, C. 2011, ApJ, 737, L37
Avila-Reese, V., Colín, P., Gottlöber, S., Firmani, C., & Maulbetsch, C. 2005, ApJ, 634, 51
Behroozi, P. S., Conroy, C., & Wechsler, R. H. 2010, ApJ, 717, 379
Bertschinger, E. 2011, GRAFIC-2: Multiscale Gaussian Random Fields for Cosmological Simulations, Astrophysics Source Code Library
Bett, P., Eke, V., Frenk, C. S., Jenkins, A., & Okamoto, T. 2010, MNRAS, 404, 1137
Binney, J. 1977, ApJ, 215, 483
Bouché et al. 2012, MNRAS, 426, 801
—. 2013, Science, 341, 50
—. 2016, ApJ, 820, 121
Bray et al. 2015, ArXiv:1508.05393
Brook et al. 2008, ApJ, 689, 678
—. 2011a, MNRAS, 415, 1051
—. 2011b, MNRAS, 415, 1051
Brooks et al. 2009, ApJ, 694, 396
Bryan et al. 2014, ApJS, 211, 19
Bullock, J. S., Dekel, A., Kolatt, T. S., Kravtsov, A. V., Klypin, A. A., Porciani, C., & Primack, J. R. 2001, ApJ, 555, 240
Cantalupo, S., Arrigoni-Battaia, F., Prochaska, J. X., Hennawi, J. F., & Madau, P. 2014, Nature, 506, 63
Cen, R., Nagamine, K., & Ostriker, J. P. 2005, ApJ, 635, 86
Ceverino, D., Dekel, A., & Bournaud, F. 2010, MNRAS, 404, 2151
Ceverino, D. & Klypin, A. 2009, ApJ, 695, 292
Ceverino, D., Klypin, A., Klimek, E. S., Trujillo-Gomez, S., Churchill, C. W., Primack, J., & Dekel, A. 2014, MNRAS, 442, 1545
Ceverino, D., Primack, J., & Dekel, A. 2015, MNRAS, 453, 408
Ceverino et al. 2015, ArXiv:1511.07653
—. 2016, MNRAS, 457, 2605
Chan et al. 2015, ArXiv:1507.02282
Chen, D. N., Jing, Y. P., & Yoshikaw, K. 2003, ApJ, 597, 35
Chisari et al. 2015, ArXiv:1507.07843
Christlein, D. & Zaritsky, D. 2008, ApJ, 680, 1053
Codis, S., Pichon, C., & Pogosyan, D. 2015, MNRAS, 452, 3369
Codis et al. 2012, MNRAS, 427, 3320
Courtois, H. M., Zaritsky, D., Sorce, J. G., & Pomarède, D. 2015, MNRAS, 448, 1767
Crighton, N. H. M., Hennawi, J. F., & Prochaska, J. X. 2013, ApJ, 776, L18
Cullen, L. & Dehnen, W. 2010, MNRAS, 408, 669
Dalgarno, A. & McCray, R. A. 1972, ARA&A, 10, 375
Danovich, M., Dekel, A., Hahn, O., Ceverino, D., & Primack, J. 2015, MNRAS, 449, 2087
Danovich, M., Dekel, A., Hahn, O., & Teyssier, R. 2012, MNRAS, 422, 1732
Dekel, A. & Birnboim, Y. 2006, MNRAS, 368, 2
Dekel et al. 2009, Nature, 457, 451
Diamond-Stanic et al. 2015, ArXiv:1507.01945
D'Onghia, E. & Navarro, J. F. 2007, MNRAS, 380, L58
Dubois, Y. & Teyssier, R. 2008, A&A, 477, 79
Dubois et al. 2014, MNRAS, 444, 1453
Fall, S. M. & Efstathiou, G. 1980, MNRAS, 193, 189
Faucher-Giguère, C.-A., Hopkins, P. F., Kereš, D., Muratov, A. L., Quataert, E., & Murray, N. 2015, MNRAS, 449, 987
Faucher-Giguère, C.-A. & Kereš, D. 2011, MNRAS, 412, L118
Faucher-Giguère, C.-A., Kereš, D., & Ma, C.-P. 2011, MNRAS, 417, 2982
Faucher-Giguère, C.-A., Lidz, A., Zaldarriaga, M., & Hernquist, L. 2009, ApJ, 703, 1416
Fernández, X., Joung, M. R., & Putman, M. E. 2012, ApJ, 749, 181
García-Ruiz, I., Sancisi, R., & Kuijken, K. 2002, A&A, 394, 769
Genel et al. 2014, MNRAS, 445, 175
—. 2015, ApJ, 804, L40
Gnedin et al. 2011, ArXiv:1108.5736
Goerdt, T. & Ceverino, D. 2015, MNRAS, 450, 3359
Greggio, L. & Renzini, A. 1983, A&A, 118, 217
Haardt, F. & Madau, P. 1996, ApJ, 461, 20
Hahn, O., Teyssier, R., & Carollo, C. M. 2010, MNRAS, 405, 274
Hobbs, A., Read, J., & Nicola, A. 2015, MNRAS, 452, 3593
Holwerda, B. W., Pirzkal, N., & Heiner, J. S. 2012, MNRAS, 427, 3159
Hopkins, P. F. 2013, MNRAS, 428, 2840
—. 2015, MNRAS, 450, 53
Hopkins, P. F., Narayanan, D., & Murray, N. 2013, MNRAS, 432, 2647
Hopkins, P. F. e. a. 2010, ApJ, 724, 915
Hopkins et al. 2014, MNRAS, 445, 581
Huang et al. 2014, ApJ, 793, 40
Ishiyama et al. 2013, ApJ, 767, 146
Joung, M. R., Mac Low, M.-M., & Bryan, G. L. 2009, ApJ, 704, 137
Joung, M. R., Putman, M. E., Bryan, G. L., Fernández, X., & Peek, J. E. G. 2012, ApJ, 759, 137
Kacprzak, G. G., Churchill, C. W., Ceverino, D., Steidel, C. C., Klypin, A., & Murphy, M. T. 2010, ApJ, 711, 533
Kacprzak, G. G., Churchill, C. W., & Nielsen, N. M. 2012a, ApJ, 760, L7
Kacprzak, G. G., Churchill, C. W., Steidel, C. C., Spitler, L. R., & Holtzman, J. A. 2012b, MNRAS, 427, 3029
Katz, N., Weinberg, D. H., & Hernquist, L. 1996, ApJS, 105, 19
Kay, S. T., Pearce, F. R., Frenk, C. S., & Jenkins, A. 2002, MNRAS, 330, 113
Kereš, D. & Hernquist, L. 2009, ApJ, 700, L1
Kereš, D., Katz, N., Fardal, M., Davé, R., & Weinberg, D. H. 2009, MNRAS, 395, 160
Kereš, D., Katz, N., Weinberg, D. H., & Davé, R. 2005, MNRAS, 363, 2

Kim, J., Choi, Y.-Y., Kim, S. S., & Lee, J.-E. 2015, ArXiv:1508.06037
Kim et al. 2014, ApJS, 210, 14
Kimm, T., Devriendt, J., Slyz, A., Pichon, C., Kassin, S. A., & Dubois, Y. 2011, ArXiv:1106.0538
Komatsu et al. 2009, ApJS, 180, 330
Kravtsov, A. V. 2003, ApJ, 590, L1
Kravtsov, A. V., Klypin, A. A., & Khokhlov, A. M. 1997, ApJS, 111, 73
Kroupa, P. 2001, MNRAS, 322, 231
Krumholz, M. R. & Gnedin, N. Y. 2011, ApJ, 729, 36
Leitherer et al. 1999, ApJS, 123, 3
—. 2010, ApJS, 189, 309
Lemonias et al. 2011, ApJ, 733, 74
Ma et al. 2015, MNRAS, 453, 960
Macciò, A. V., Moore, B., & Stadel, J. 2006, ApJ, 636, L25
Maller, A. H. & Bullock, J. S. 2004, MNRAS, 355, 694
Maller, A. H. & Dekel, A. 2002, MNRAS, 335, 487
Maller, A. H., Dekel, A., & Somerville, R. 2002, MNRAS, 329, 423
Mandelker et al. 2015, ArXiv:1512.08791
Marasco, A., Debattista, V. P., Fraternali, F., van der Hulst, T., Wadsley, J., Quinn, T., & Roškar, R. 2015, MNRAS, 451, 4223
Martin et al. 2014, ApJ, 786, 107
—. 2015, Nature, 524, 192
—. 2016, ApJ, 824, L5
Martizzi, D., Teyssier, R., Moore, B., & Wentz, T. 2012, MNRAS, 422, 3081
Mistani et al. 2015, ArXiv:1509.00030
Mo, H. J., Mao, S., & White, S. D. M. 1998, MNRAS, 295, 319
Morris, J. P. 1996, Publications Astronomical Society of Australia, 13, 97
Muñoz-Cuartas, J. C., Macciò, A. V., Gottlöber, S., & Dutton, A. A. 2011, MNRAS, 411, 584
Muratov et al. 2015, MNRAS, 454, 2691
Nelson, D., Genel, S., Pillepich, A., Vogelsberger, M., Springel, V., & Hernquist, L. 2016, MNRAS
Nelson, D., Genel, S., Vogelsberger, M., Springel, V., Sijacki, D., Torrey, P., & Hernquist, L. 2015, MNRAS, 448, 59
Nelson, D., Vogelsberger, M., Genel, S., Sijacki, D., Kereš, D., Springel, V., & Hernquist, L. 2013, MNRAS, 429, 3353
Nielsen, N. M., Churchill, C. W., Kacprzak, G. G., Murphy, M. T., & Evans, J. L. 2015, ArXiv:1505.07167
Oñorbe et al. 2015, ArXiv:1502.02036
Ocvirk, P., Pichon, C., & Teyssier, R. 2008, MNRAS, 390, 1326
Oosterloo et al. 2007, A&A, 465, 787
Pakmor et al. 2016, MNRAS, 455, 1134
Pichon, C., Pogosyan, D., Kimm, T., Slyz, A., Devriendt, J., & Dubois, Y. 2011, MNRAS, 418, 2493
Piontek, F. & Steinmetz, M. 2011, MNRAS, 410, 2625
Prescott, M. K. M., Martin, C. L., & Dey, A. 2015, ApJ, 799, 62
Prieto, J., Jimenez, R., Haiman, Z., & González, R. E. 2015, MNRAS, 452, 784
Putman, M. E., Peek, J. E. G., & Joung, M. R. 2012, ARA&A, 50, 491
Rees, M. J. & Ostriker, J. P. 1977, MNRAS, 179, 541
Richardson et al. 2016, arxiv:1605.03589
Rodriguez-Gomez et al. 2015, MNRAS, 449, 49
Sales et al. 2015, MNRAS, 447, L6
Sancisi, R., Fraternali, F., Oosterloo, T., & van der Hulst, T. 2008, A&A Rev., 15, 189
Scannapieco et al. 2012, MNRAS, 423, 1726
Schaye, J. 2001, ApJ, 562, L95
Sharma, S. & Steinmetz, M. 2005, ApJ, 628, 21
Silk, J. 1977, ApJ, 211, 638
Snyder et al. 2015a, MNRAS, 451, 4290
—. 2015b, ArXiv:1502.07747
Spavone, M., Iodice, E., Arnaboldi, M., Gerhard, O., Saglia, R., & Longo, G. 2010, ApJ, 714, 1081
Springel, V. 2010, MNRAS, 401, 791
Springel, V. & Hernquist, L. 2003, MNRAS, 339, 289
Stewart, K. R., Bullock, J. S., Wechsler, R. H., & Maller, A. H. 2009, ApJ, 702, 307
Stewart et al. 2011a, ApJ, 735, L1
—. 2011b, ApJ, 738, 39
—. 2013, ApJ, 769, 74
Tacchella et al. 2016a, MNRAS, 458, 242
—. 2016b, MNRAS, 457, 2790
Teyssier, R. 2002, A&A, 385, 337
Thacker, R. J. & Couchman, H. M. P. 2000, ApJ, 545, 728
Thilker et al. 2005, ApJ, 619, L79
—. 2007, ApJS, 173, 538
Tillson, H., Devriendt, J., Slyz, A., Miller, L., & Pichon, C. 2015, MNRAS, 449, 4363
Tomassetti et al. 2016, MNRAS, 458, 4477
Torrey, P., Vogelsberger, M., Sijacki, D., Springel, V., & Hernquist, L. 2012, MNRAS, 427, 2224
Torrey et al. 2014, MNRAS, 438, 1985
—. 2015a, ArXiv:1507.01942
—. 2015b, MNRAS, 447, 2753
Trowland, H. E., Lewis, G. F., & Bland-Hawthorn, J. 2013, ApJ, 762, 72
Turk, M. J. 2013, ArXiv:1301.7064
Turk, M. J. & Smith, B. D. 2011, ArXiv:1112.4482
Turk et al. 2011, ApJS, 192, 9
van de Voort, F., Schaye, J., Booth, C. M., Haas, M. R., & Dalla Vecchia, C. 2011, MNRAS, 414, 2458
van de Voort et al. 2015, MNRAS, 451, 3269
Vitvitska, M., Klypin, A. A., Kravtsov, A. V., Wechsler, R. H., Primack, J. R., & Bullock, J. S. 2002, ApJ, 581, 799
Vogelsberger, M., Genel, S., Sijacki, D., Torrey, P., Springel, V., & Hernquist, L. 2013, MNRAS, 436, 3031
Vogelsberger et al. 2013, MNRAS, 436, 3031
—. 2014, MNRAS, 444, 1518
Wadsley, J. W., Veeravalli, G., & Couchman, H. M. P. 2008, MNRAS, 387, 427
Walter et al. 2008, AJ, 136, 2563
Wang et al. 2013, ArXiv:1303.3538
Welker, C., Devriendt, J., Dubois, Y., Pichon, C., & Peirani, S. 2014, MNRAS, 445, L46
Wellons et al. 2015a, ArXiv:1507.02291
—. 2015b, MNRAS, 449, 361
Wheeler et al. 2015, MNRAS, 453, 1305
White, S. D. M. & Frenk, C. S. 1991, ApJ, 379, 52
White, S. D. M. & Rees, M. J. 1978, MNRAS, 183, 341
Wiersma, R. P. C., Schaye, J., & Smith, B. D. 2009a, MNRAS, 393, 99
Wiersma, R. P. C., Schaye, J., Theuns, T., Dalla Vecchia, C., & Tornatore, L. 2009b, MNRAS, 399, 574
Zahid et al. 2014, Ap&SS, 349, 873
Zolotov et al. 2015, MNRAS, 450, 2327